Nano-Micro Letters

ISSN 2311-6706
e-ISSN 2150-5551
CN 31-2103/TB

ARTICLE

https://doi.org/10.1007/s40820-019-0296-7

Cite as
Nano-Micro Lett.
(2019) 11:65

Received: 5 June 2019
Accepted: 16 July 2019
Published online: 2 August 2019
© The Author(s) 2019

Electrostatic Self-assembly of 0D–2D SnO_2 Quantum Dots/$Ti_3C_2T_x$ MXene Hybrids as Anode for Lithium-Ion Batteries

Huan Liu[1], Xin Zhang[2], Yifan Zhu[2], Bin Cao[2], Qizhen Zhu[2], Peng Zhang[2], Bin Xu[2] ✉, Feng Wu[1], Renjie Chen[1] ✉

Huan Liu and Xin Zhang have contributed equally to this work.

✉ Bin Xu, binxumail@163.com; Renjie Chen, chenrj@bit.edu.cn

[1] School of Materials Science and Engineering, Beijing Key Laboratory of Environmental Science and Engineering, Beijing Institute of Technology, Beijing 100081, People's Republic of China

[2] State Key Laboratory of Organic-Inorganic Composites, Beijing Key Laboratory of Electrochemical Process and Technology for Materials, Beijing University of Chemical Technology, Beijing 100029, People's Republic of China

HIGHLIGHTS

- 0D–2D SnO_2 quantum dots/MXene (SnO_2 QDs/MXene) hybrids were synthesized by electrostatic self-assembly.
- MXene not only provides efficient pathways for fast transport of electrons and Li ions, but also buffers the volume change of SnO_2 during charge/discharge process.
- The 0D–2D SnO_2 QDs/MXene hybrids deliver high capacity, excellent cycle and rate performances as anode of lithium-ion batteries.

ABSTRACT MXenes, a new family of two-dimensional (2D) materials with excellent electronic conductivity and hydrophilicity, have shown distinctive advantages as a highly conductive matrix material for lithium-ion battery anodes. Herein, a facile electrostatic self-assembly of SnO_2 quantum dots (QDs) on $Ti_3C_2T_x$ MXene sheets is proposed. The as-prepared SnO_2/MXene hybrids have a unique 0D–2D structure, in which the 0D SnO_2 QDs (~ 4.7 nm) are uniformly distributed over 2D $Ti_3C_2T_x$ MXene sheets with controllable loading amount. The SnO_2 QDs serve as a high capacity provider and the "spacer" to prevent the MXene sheets from restacking; the highly conductive $Ti_3C_2T_x$ MXene can not only provide efficient pathways for fast transport of electrons and Li ions, but also buffer the volume change of SnO_2 during lithiation/delithiation by confining SnO_2 QDs between the MXene nanosheets. Therefore, the 0D–2D SnO_2 QDs/MXene hybrids deliver superior lithium storage properties with high capacity (887.4 mAh g^{-1} at 50 mA g^{-1}), stable cycle performance (659.8 mAh g^{-1} at 100 mA g^{-1} after 100 cycles with a capacity retention of 91%) and excellent rate performance (364 mAh g^{-1} at 3 A g^{-1}), making it a promising anode material for lithium-ion batteries.

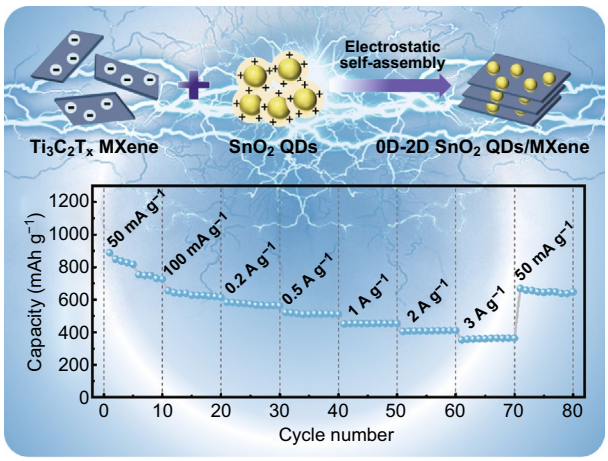

KEYWORDS MXene; SnO_2; Quantum dots; 0D–2D hybrid; Lithium-ion battery

1 Introduction

Lithium-ion batteries (LIBs) are widely used in various portable electronics, electric tools, and electric vehicles due to their high energy density, long cycle life, and environmental friendly [1, 2]. Nevertheless, the conventional graphite anode of LIBs with a specific capacity of 372 mAh g^{-1} can hardly meet the rapidly increasing demand of high energy density. Great efforts have been made to develop promising anode materials with high capacity, such as transition metal oxides [3, 4], alloys [5, 6], metal oxides/sulfates [7–9], and phosphorous [10–12]. Among various metal oxides, SnO_2 has attracted a lot of attention due to its relatively high theoretical capacity (790 mAh g^{-1}, which is twice than the currently used graphite), low average working potential (~ 0.6 V vs. Li^+/Li), natural abundance and low price [13–16]. Unfortunately, its practical application as anode material in LIBs is seriously limited by the poor cycle stability resulting from the severe volume change (> 300 vol%) during the charge/discharge process. Meanwhile, SnO_2 also suffers from low electrical conductivity, resulting in poor rate capability. To improve the electrochemical performances of SnO_2, several strategies have been proposed to overcome these issues. One of the effective way is to fabricate nanostructured SnO_2, such as SnO_2 quantum dots (QDs) [17], SnO_2 hollow spheres [18], or SnO_2 nanowires [19], which could restrain the structure changes during lithium alloying and shorten the ion diffusion lengths [20]. The other way is to combine SnO_2 with various carbon materials possessing high conductivity such as carbon nanotubes, carbon fiber or graphene [21–26]. The conductive carbon can not only improve the overall electrical conductivity of the composites but also act as a buffer to slow down the structure collapse of the electrode.

MXenes are a newly emerging family of 2D materials with a general formula of $M_{n+1}X_nT_x$, where M represents early transition metal (M = Ti, Sr, V, Cr, Ta, Nb, Zr, Mo, and H_f), X is carbon and/or nitrogen, and T stands for the surface termination groups (–OH, –F=O) [27–31]. Due to their excellent electrical conductivity, tailorable surface chemistries, and mechanical properties, MXenes have recently attracted great interests in energy storage devices such as LIBs, sodium-ion batteries, and supercapacitors [32–35]. Particularly, as one of the most widely studied MXenes, $Ti_3C_2T_x$ is a potential anode material for LIBs, which can deliver excellent cycle stability and superior rate performances. However, the theoretical reversible capacity of $Ti_3C_2T_x$ is only 320 mAh g^{-1} [36]. On the other hand, MXene can also be used as a substrate to fabricate hybrids with other active materials, including metal oxides, which have higher theoretical capacity but poor conductivity and are prone to large volume change during charge/discharge. In the hybrids, MXene can improve the conductivity and buffer the volume changes of the metal oxide, while the metal oxide provides high capacity. Thus, the MXene/metal oxide hybrid could achieve high capacity, stable cycle and good rate performance [37–41]. For example, $Ti_3C_2T_x/Fe_2O_3$ nanocomposite was prepared by confining Fe_2O_3 nanoparticles into $Ti_3C_2T_x$ nanosheets through ball-milling method, which showed reversible capacities of ~ 203 mAh g^{-1} at 1 C and 100 mAh g^{-1} at 10 C [37]. MXene/$NiCo_2O_4$ composite with a capacity reaching up to 1330 mAh g^{-1} was synthesized by spray coating method [38]. Some recent works indicate that MXene is also a good substrate to improve the lithium storage performance of SnO_2. The hybrids of SnO_2 with MXene prepared by wet hydrothermal approach has shown a high capacity of 1021 mAh g^{-1} and improved cycle stability [40]. However, a few reports indicate that MXene is unavoidable to be oxidized to titanium dioxide (TiO_2) as a by-product during these processes, thereby, influencing the electrochemical performance of the composites. Recently, our group proposed a general route to self-assemble transition metal oxide nanostructures on $Ti_3C_2T_x$ MXene nanosheets through van der Waals interaction. The proposed method allowed fabrication of hybrids without getting MXene to be oxidized and achieved enhanced cycle and rate performance [15].

In this work, a simple method is proposed to prepare 0D–2D SnO_2 QDs/MXene hybrids by electrostatic self-assembling SnO_2 QDs on the surface of 2D $Ti_3C_2T_x$ MXene nanosheets under ultrasonication. Since, the synthesis is accomplished in a very mild condition, i.e., ultrasonication treatment of the mixture of negatively charged MXene and positively charged SnO_2 QDs at room temperature, the MXene oxidation is effectively avoided. In the hybrids, 2D nanosheet of MXene acts as a substrate to support 0D SnO_2 QDs, which can not only provide large electrode/electrolyte interface area for fast reversible transport of electrons and ions, but could also inhibit the aggregation of SnO_2 QDs and buffer the volume changes during charge/discharge process. The SnO_2 QDs with ultra-small particle size can effectively maximize the activity and specific capacity and minimize

© The authors
https://doi.org/10.1007/s40820-019-0296-7

the volume change while inhibiting the structure collapse during charge/discharge process and shortening the lithium diffusion pathways. In addition, the SnO_2 QDs acts as a "spacer" to prevent the MXene nanosheets from restacking and thus protecting the Li^+ migration channels and active sites. These unique features endow the 0D–2D SnO_2 QDs/MXene hybrids with high lithium storage capacity, excellent cycle stability and superior rate performance, indicating a promising anode for LIBs.

2 Experimental

2.1 Synthesis of $Ti_3C_2T_x$ MXene

The $Ti_3C_2T_x$ MXene was synthesized by etching Ti_3AlC_2 (400 mesh, purchased from Yiyi Technology Co., Ltd.) with LiF + HCl solution as reported previously [41]. Typically, 1.0 g Ti_3AlC_2 powder was subjected to a mixture containing LiF (1.0 g) and hydrochloric acid (12 M, 10 mL) under stirring conditions for 24 h at 35 °C. After several times of centrifugation-washing with deionized (DI) water, the product was then dispersed in 50 mL DI water, stored under ultrasound for 30 min. The dark green supernatant was collected by centrifugation at 3500 rpm for 1 h. Finally, the black MXene liquid was obtained and sealed for future use.

2.2 Synthesis of SnO_2 QDs

In order to obtain SnO_2 QDs, 4 mmol $SnCl_2{\cdot}2H_2O$ and 4 mmol thiourea (CH_4N_2S) were added to 30 mL DI water and magnetically stirred at room temperature to form a milky suspension. After stirring for 24 h, a clear yellow aqueous solution containing SnO_2 QDs was obtained.

2.3 Synthesis of 0D–2D SnO_2 QDs/MXene Hybrids

In a typical synthesis, 5 mL of as-prepared SnO_2 QDs solution was added to 40 mg 0.1 mg mL^{-1} $Ti_3C_2T_x$ MXene solution under ultrasonication for 6 h. The SnO_2 QDs were deposited on the $Ti_3C_2T_x$ layers during this process and solid–liquid separation was observed. Finally, the black precipitate of SnO_2 QDs/MXene hybrids were collected by vacuum filtration, washed with water and dried in a vacuum oven at 80 °C for 6 h. The above hybrid was denoted as SnO_2 QDs/MXene-52. For comparison, we also prepared another SnO_2 QDs/$Ti_3C_2T_x$ hybrids (SnO_2 QDs/MXene-51) under the same conditions, but the addition amount of MXene in this solution was 20 mg.

2.4 Materials Characterization

Scanning electron microscopy (SEM) characterization was conducted using a Gemini SEM 500. Transmission electron microscopy (TEM) characterization was conducted on a JEOL JEM-F200 (HR) equipped with selected area electron diffraction (SAED). X-ray diffraction (XRD) patterns were recorded on a Bruker D8 ADVANCE with monochromatic Cu Kα radiation ($\lambda = 1.54060$ Å). Raman spectra were obtained with a LabRAM HR Evolution Raman spectrometer (633 nm). X-ray photoelectron spectroscopy (XPS) analysis was performed using a Thermo Fisher ESCALAB Xi^+ to analyze the chemical compositions of the samples.

2.5 Electrochemical Measurements

The working electrodes were prepared by mixing 80 wt% active material, 10 wt% Super P and 10 wt% carboxymethylated cellulose (CMC) in DI water. After coating the slurry on the copper foil, the electrodes were dried at 60 °C in vacuum oven for 8 h to remove the solvent. To test electrochemical performances, CR2025-type coin cells were assembled in an argon-filled glove box (Mikrouna, H_2O, $O_2 < 0.1$ ppm) using Li foil as half-cell counter electrode, and microporous membrane (Celgard 2400) as separator. The electrolyte was 1 M $LiPF_6$ in a mixture of ethylene carbonate (EC)/diethyl carbonate (DEC)/dimethyl carbonate (DMC) with a volume ratio of 1:1:1. The charge/discharge (GCD) tests were performed using a LAND BT2000 battery tester. The potential window was 0.01–2.5 V versus Li/Li^+. The CV traces were recorded on a CS350 electrochemical workstation from 0.01 to 2.5 V. Electrochemical impedance spectroscopy (EIS) measurements were performed on the VSP Bio-Logic SAS at frequencies ranging from 10 mHz to 100 kHz with an applied AC signal amplitude of 10 mV. The capacities of the samples were calculated based on all the components in the active materials, i.e., the mass of SnO_2 QDs/$Ti_3C_2T_x$ hybrids.

3 Results and Discussion

The synthesis route for 0D–2D SnO_2 QDs/MXene by electrostatic self-assembly is illustrated in Fig. 1. Firstly, transparent yellow aqueous solution of positively charged SnO_2 QDs is prepared by hydrolysis, dehydration and oxidation of $SnCl_2{\cdot}2H_2O$ in DI water, where thiourea is added as a promoter and stabilizer (Fig. S1a). The mercaptan group can easily bound to Sn^{2+}, and the SnO_2 QDs whose zeta potential is +99.0 mV (Fig. S1b) is surrounded by a positively charged protic amino group ($–NH_3^+$), which makes it highly stable and electropositive [42]. The $Ti_3C_2T_x$ MXene solution with its negatively charged groups (–F, –OH) [43], and zeta potential of − 36.2 mV, is very stable in water (Fig. S1a) due to the hydrophilicity and electrostatic repulsion between neighboring nanosheets. When positively charged SnO_2 QDs are added into the negatively charged $Ti_3C_2T_x$ colloidal solution, the SnO_2 QDs can easily load onto the surface of the MXene nanosheets. After the continuous ultrasonication of 6 h, the supernatant becomes clear and colorless, and black precipitates are obtained. The positively charged SnO_2 QDs are captured by the negatively charged MXene nanosheets only by ultrasonic treatment without other components and additional treatments, implying an electrostatic self-assembly mechanism for the designed 0D–2D SnO_2 QDs/MXene hybrids. The $Ti_3C_2T_x$ MXene with 2D layered structure as a conductive matrix facilitates the charge transfer and accommodates the volume change of SnO_2 QDs; the SnO_2 QDs thus prevents the MXene nanosheets from restacking by working as "spacer" and providing channels for fast transfer of Li ion with promising electrochemical performance.

SEM and TEM were employed to characterize the morphology and structure of the as-prepared samples. The pure $Ti_3C_2T_x$ (Fig. S1c) displays a compact 2D layered structure. After decoration with SnO_2 QDs, the SnO_2 QDs/MXene hybrids exhibit 0D–2D structure, as shown in Fig. 2a. From

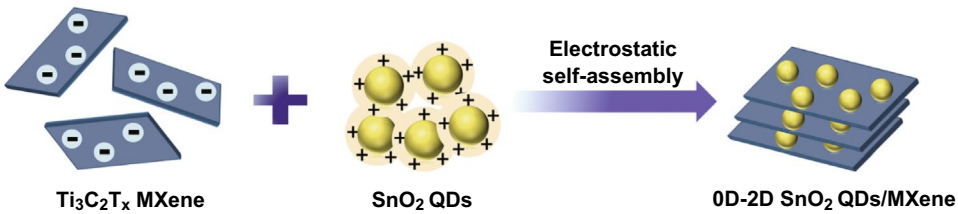

Fig. 1 Schematic illustration for the preparation of 0D–2D SnO_2 QDs/MXene hybrids

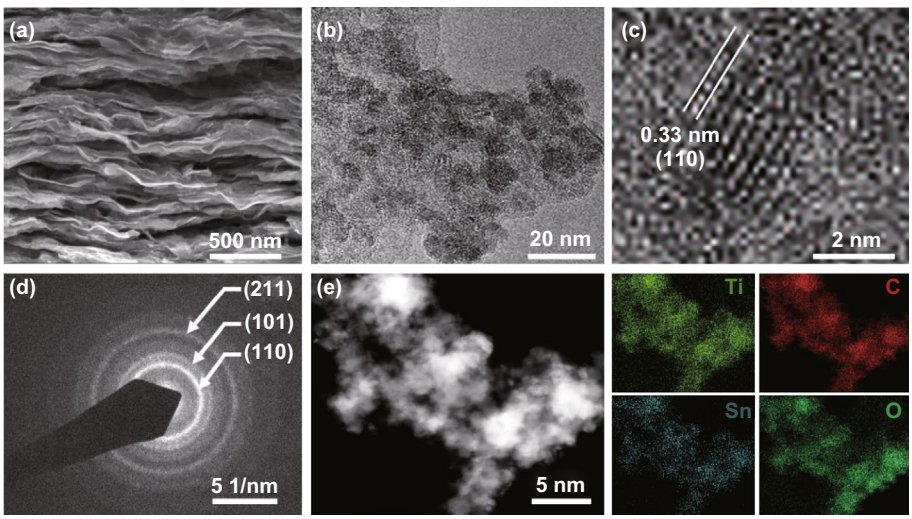

Fig. 2 **a** SEM image, **b** TEM image, **c** HRTEM image of 0D–2D SnO_2 QDs/MXene hybrid. **d** SAED patterns of SnO_2 QDs. **e** STEM image and corresponding elemental mapping images of Ti, C, Sn, and O

© The authors
https://doi.org/10.1007/s40820-019-0296-7

a closer view in Fig. 2b, it can be seen that the spatially dispersed SnO_2 QDs are evenly distributed over the surface of the MXene nanosheets. The particle-size distribution analysis (Fig. S1d) indicates the SnO_2 QDs have an average particle size of ~4.5 nm, favoring the electrode/electrolyte interactions. Since the diffusion of Li ions is strongly dependent on the transport length and the active sites, the ultra-small particle size of SnO_2 QDs can not only expose a large number of electrochemical active sites shuttling Li ions in and out, but also shorten the diffusion path of Li ion transport, which are beneficial for improving the capacity and rate performance. Figure 2c shows clear lattice fringes of the SnO_2 QDs, indicating a high degree of crystallinity. The crystal lattice with a spacing of 0.33 nm is consistent with the d spacing of (110) planes of the SnO_2 tetragonal phase. The selected area electron diffraction (SAED) pattern (Fig. 2d) shows clear diffraction rings, implying the polycrystalline nature of SnO_2. These diffraction rings can be well indexed to the (110), (101), and (211) planes of SnO_2. Moreover, the typical scanning TEM (STEM) and elemental mapping images of SnO_2 QDs/MXene hybrid (Fig. 2e) show homogeneously distributed Ti, C, Sn, and O elements, demonstrating the uniform loading of SnO_2 QDs on the surface of MXene sheets.

The phase structures of the as-prepared SnO_2 QDs/MXene hybrids were verified by XRD as shown in Fig. 3a. $Ti_3C_2T_x$ exhibits the major peaks, such as the (002), (006), (008), (0010), and (0012) [44]. Typically, the (002) plane of the $Ti_3C_2T_x$ MXene is located at $2\theta = 6.4°$, corresponding to an interplanar spacing of 13.7 Å [45]. In addition, the pure tetragonal phase of crystalline SnO_2 (JCPDS No. 41-1445) is located at 26.5°, 34.1°, and 52.4°, corresponding to (110), (101), and (211). The XRD patterns of the SnO_2 QDs/MXene hybrids consist of $Ti_3C_2T_x$ and tetragonal phase SnO_2, indicating that SnO_2 QDs/MXene hybrids have successfully formed. No any extra crystalline phase peaks such as TiO_2 are observed, indicating the electrostatic self-assembly process is mild with no oxidation of MXene. In addition, the (002) peak of the SnO_2–MXene composite (Fig. S1e) was downshifted compared to pure MXene, indicating increased interlayer spacing of the MXene in the hybrids.

Raman spectra further confirm the phase characteristics of the SnO_2 QDs/MXene-52 hybrid. As shown in Figs. 3b and S1f, the peaks of pure SnO_2 at 271, 465, and 698 cm^{-1} can be assigned to the E_g and A_{1g} active mode of SnO_2, respectively [46]. Moreover, the pure MXene exhibits a peak at 199 cm^{-1} which corresponds to the A_{1g} symmetry out-of-plane vibrations of Ti atoms, whereas the peaks at 381 and 622 cm^{-1} are related to the E_g group vibrations, including in-plane (shear) modes of Ti, C, and surface functional group atoms [47]. For the SnO_2 QDs/MXene-52, the spectrum manifests six cognizable Raman-active modes, combining the characteristic Raman peaks of $Ti_3C_2T_x$ and SnO_2. In comparison with the pure SnO_2, the peak intensity of SnO_2 in the hybrid has significantly declined. This suggests that the SnO_2 QDs are well separated by the $Ti_3C_2T_x$ nanosheets, which weakens the Raman signal from the SnO_2. It's worth noting that no strong peak for TiO_2 was detected at 144 cm^{-1}, confirming that MXene has not oxidized during the hybrid formation.

The elemental composition of SnO_2 QDs/MXene hybrid was further analyzed by XPS. For pristine $Ti_3C_2T_x$ MXene, there are only four main elements, Ti, C, F, and O, whereas for SnO_2 QDs/MXene-52, the Sn element is also detected, indicating the presence of SnO_2 in the hybrid (Fig. S2a). In the high-resolution C 1*s* spectrum (Fig. 3c), the characteristic peaks correspond to C–Ti (284.2 eV), C–C (288.7 eV), C–O (288.1 eV), C=O (289.5 eV), and O–C=O (291.6 eV) [48]. The particular peak located at 282.1 eV can be assigned to the C–Ti bond in $Ti_3C_2T_x$ sheets. The XPS spectrum of the Ti 2*p* (Fig. 3d) reveals that peaks of Ti bound to C, Ti(II), and Ti(III). The Ti–C $2p_{3/2}$, Ti(II) $2p_{3/2}$, Ti(III) $2p_{3/2}$, T–C $2p_{1/2}$, Ti(II) $2p_{1/2}$, and Ti(III) $2p_{1/2}$ peaks are detected at binding energies of 455.1, 455.6, 456.8, 458.8, 461.3, and 462.3 eV, respectively. After loading the SnO_2 QDs, no Ti(IV) peak is observed, suggesting no oxidation of MXene in the SnO_2 QDs/MXene-52 (Fig. 3f). Meanwhile, the XPS in Sn 3*d* region has two peaks at 487.2 and 495.6 eV, which are attributed to Sn $3d_{5/2}$ and Sn $3d_{3/2}$ of SnO_2, confirming the formation of SnO_2 (Fig. S2b). Besides this, the relative intensities of Ti–C, Ti(II), and Ti(III) peaks in SnO_2 QDs/MXene-52 are relatively weaker than pure $Ti_3C_2T_x$, indicating decreasing $Ti_3C_2T_x$ signal for the hybrid. Furthermore, the slight shift of the Ti–C component to lower binding energy indicates that the synthesis of SnO_2 QDs/MXene hybrid by electrostatic attraction might have caused shift in the electron density (Fig. 3e). All of these observations demonstrate that SnO_2 QDs have been successfully deposited on the surface of the $Ti_3C_2T_x$ sheets. In addition, the introduction of SnO_2 QDs on the $Ti_3C_2T_x$ surface increases the accessible surface area [49], which is evident from the nitrogen adsorption measurements (Fig. S2c). The SnO_2 QDs/MXene-52 shows a typical type I adsorption/desorption

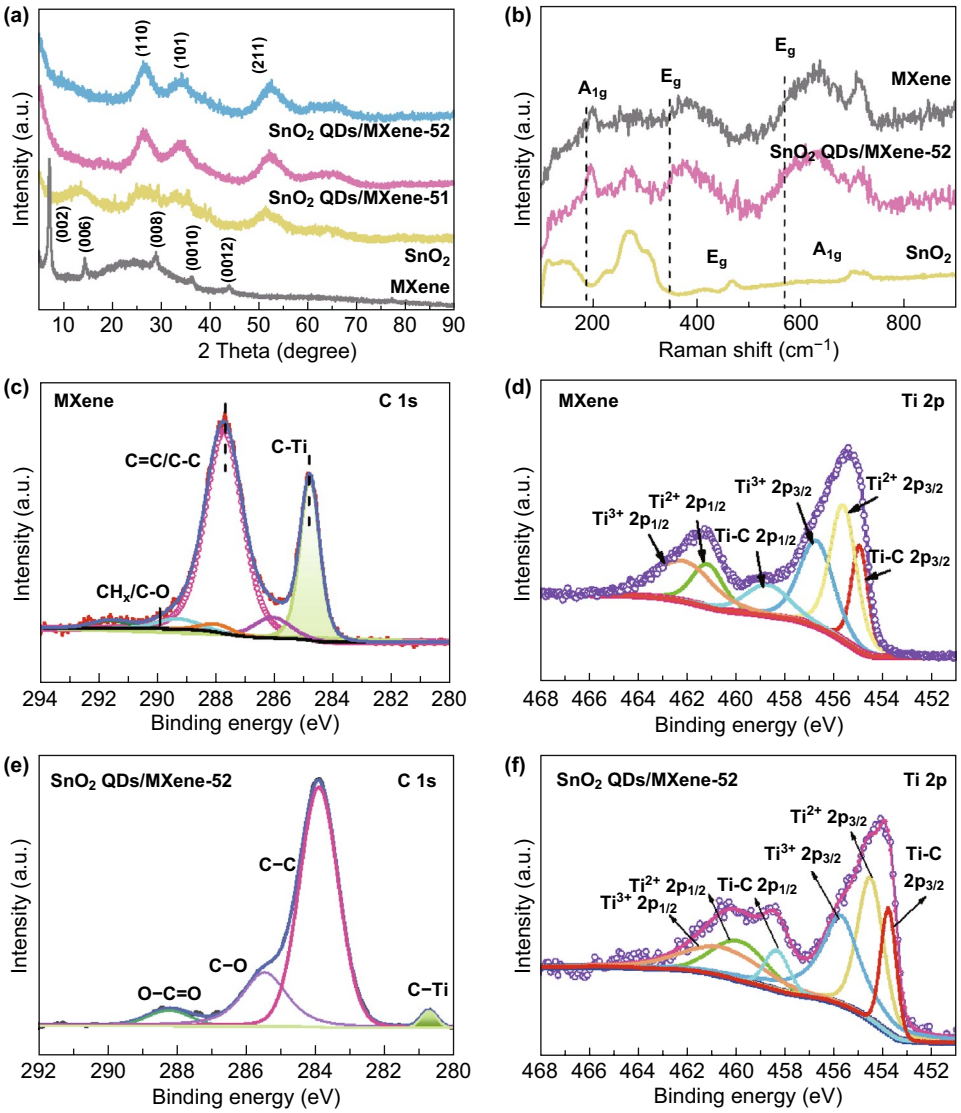

Fig. 3 **a** XRD patterns, **b** Raman spectra of MXene, SnO_2, and SnO_2 QDs/MXene hybrid. XPS spectra of **c** MXene for high-resolution C 1*s*, **d** Ti 2*p*, **e** SnO_2 QDs/MXene-52 for high-resolution C 1*s*, **f** Ti 2*p*

isotherms with a BET specific surface area of 184 $m^2\ g^{-1}$, much higher than that of the pure MXene (19 $m^2\ g^{-1}$). The large surface area is beneficial for accelerating electrolyte diffusion and accommodating volume change of the SnO_2 QDs during charge/discharge. Thus, much improved lithium storage performances could be expected.

To evaluate the electrochemical performances of the SnO_2 QDs/MXene hybrids as anode materials in LIBs, coin-type half cells were assembled using lithium as counter electrode. CV curves of $Ti_3C_2T_x$ MXene and SnO_2 QDs/MXene hybrids were scanned between 0.01 and 2.5 V. For the pure $Ti_3C_2T_x$ MXene, the broad irreversible reduction peak at around 0.7 V is observed in the first lithiation process, which is attributed to the formation of a solid electrolyte interphase (SEI) generated from the reaction of $Ti_3C_2T_x$ with Li ion [17]. In the subsequent cycles, the reversible peaks near 0.77 and 1.5 V may be the consequence of the reaction between Li^+ and the titanium-based compounds (Fig. S3a) [50]. For the pure SnO_2 QDs (Fig. S3b), the SnO_2 is considered to transform into Li_xSn ($x \leq 4.4$) and Li_2O during the initial discharge process (lithium insertion). The cathodic peak at 0.05 V result from the alloying process of Sn to Li_xSn ($0 \leq x \leq 4.4$), and the strong anode peak at about 0.5 V is caused by the de-alloying process of Li_xSn ($0 \leq x \leq 4.4$).

© The authors
https://doi.org/10.1007/s40820-019-0296-7

The anode peak at 1.2 V is caused by the partial reversible transformation of Sn to SnO_2 owing to its quantum size [51, 52]. However, in the second and third cycles of the pure SnO_2, the intensities of the cathodic and anodic peaks show continuous and significant decline, indicating rapid capacity degradation because of the structural variation of SnO_2 during lithiation/delithiation processes (Fig. S3b). The SnO_2 QDs/MXene-52 (Fig. 4a) shows CV curves with similar characteristic peaks, but the curves in the 2nd and 3rd cycles almost overlap, indicating good cycle performance. In comparison with the SnO_2 QDs/MXene-51 (Fig. 4b), the SnO_2 QDs/MXene-52 display better overlapping CV curves with the same peak positions, implying excellent reversibility in its conversion reaction.

Furthermore, the GCD profiles (Fig. 4c, d) of the SnO_2 QDs/MXene at 50 mA g^{-1} coincides well with the CV curves. The GCD profile of the $Ti_3C_2T_x$ and SnO_2 QDs electrodes were also tested at the same conditions (Fig. S3c, d). In the initial discharge profile of the SnO_2 QDs/MXene hybrids, the plateaus at 0.7 and 0.05 V correspond to the SEI formation and lithium alloying; while during the initial charge, the plateaus at 0.5 and 1.2 V relate to lithium de-alloying and partial reversible SnO_2 formation, respectively. The reversible capacity of the SnO_2 QDs/MXene-52 is 887.4 mAh g^{-1} in the first cycle, with initial Coulombic efficiency (CE) of about 51.2%. The low CE might have resulted from the SEI and Li_2O formation as well as the electrolyte decomposition. In the 5th cycle, the capacity was determined to be about 847.6 mAh g^{-1} and the corresponding CE reached about 100%. With the SEI film protection, the capacity reaches a stable state. In contrast, the SnO_2 QDs/MXene-51 delivers an initial reversible capacity of 897.5 mAh g^{-1} with a CE of 43.0% (Fig. 4d). The results indicate that the introduction of more SnO_2 QDs can increase available active sites and the capacity of the hybrid material, but at the same time cause more side reactions and reduce the initial CE, due to its ultra-small particle size and high surface area. Therefore, only appropriate ratio of SnO_2 QDs and MXene sheets could reach an optimum electrochemical performance.

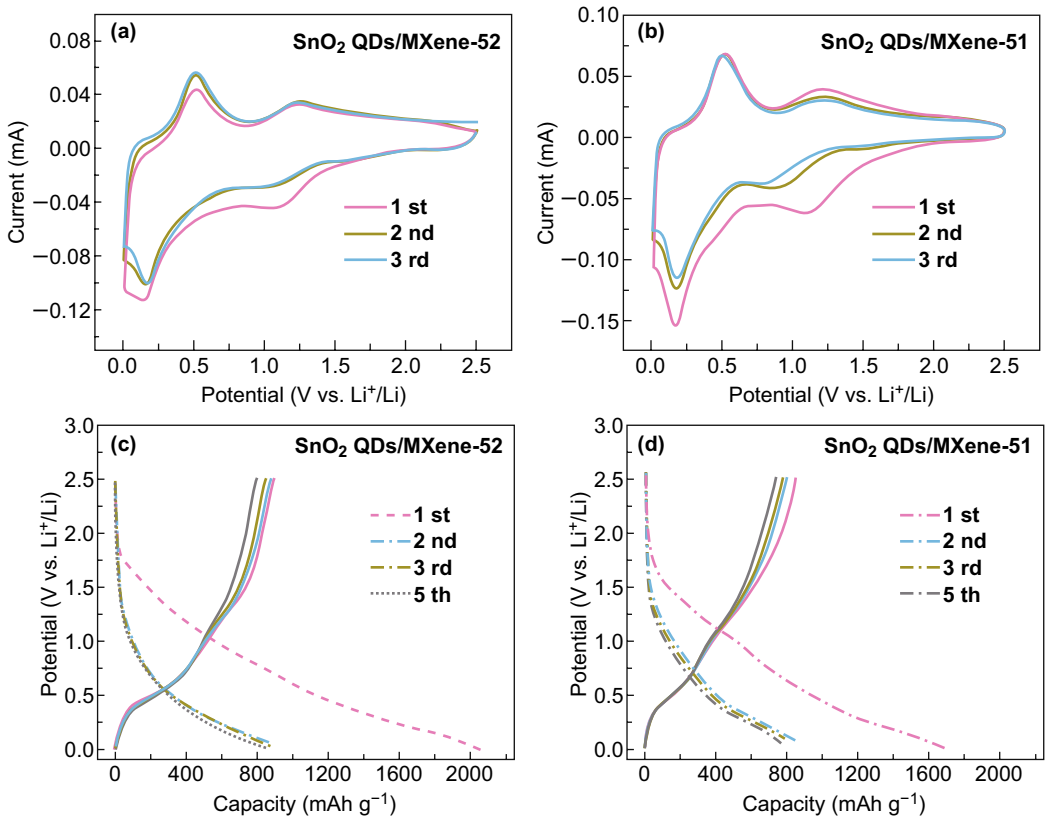

Fig. 4 Electrochemical performances as anode in LIBs. **a**, **b** CV curves of SnO_2 QDs/MXene at a scan rate of 0.1 mV s^{-1} in 0.01–2.5 V. **c**, **d** Charge/discharge curves of SnO_2 QDs/MXene at 50 mA g^{-1}

Figure 5a shows the comparison of the charge/discharge cycle performance among $Ti_3C_2T_x$ MXene, SnO_2 QDs, and SnO_2 QDs/MXene at 100 mA g^{-1}. The bare $Ti_3C_2T_x$ MXene has a low initial capacity of 79.2 mAh g^{-1} with a CE of 34.2%, which is attributed to the restacking of MXene nanosheets [36]. The initial capacity of the pure SnO_2 QDs can reach 835.9 mAh g^{-1}, but it fades very rapidly due to the severe pulverization of SnO_2 during charge/discharge. After 20 cycles, the capacity remains only 144.6 mAh g^{-1} with a capacity retention ratio of about 17% of the initial capacity. In contrast, by electrostatic self-assembly of the SnO_2 QDs on the 2D $Ti_3C_2T_x$ MXene nanosheets, the SnO_2 QDs/MXene hybrids exhibit much enhanced cycle stability. The capacity of SnO_2 QDs/MXene-52 reaches to 659.8 mAh g^{-1} with 91% retention of the initial capacity after 100 cycles, which is much higher than that of the pure SnO_2 QDs and $Ti_3C_2T_x$ MXene. In a comparative evaluation of SnO_2 QDs/MXene hybrids with different SnO_2/MXene ratio, it is found that the SnO_2 QDs/MXene-52 with abundant MXene shows better cycle stability than the SnO_2 QDs/MXene-51, indicating the importance of adequate MXene substrate in achieving optimum performance [53].

Another attractive feature of the SnO_2 QDs/MXene electrodes is the excellent rate performance. As shown in Fig. 5b,

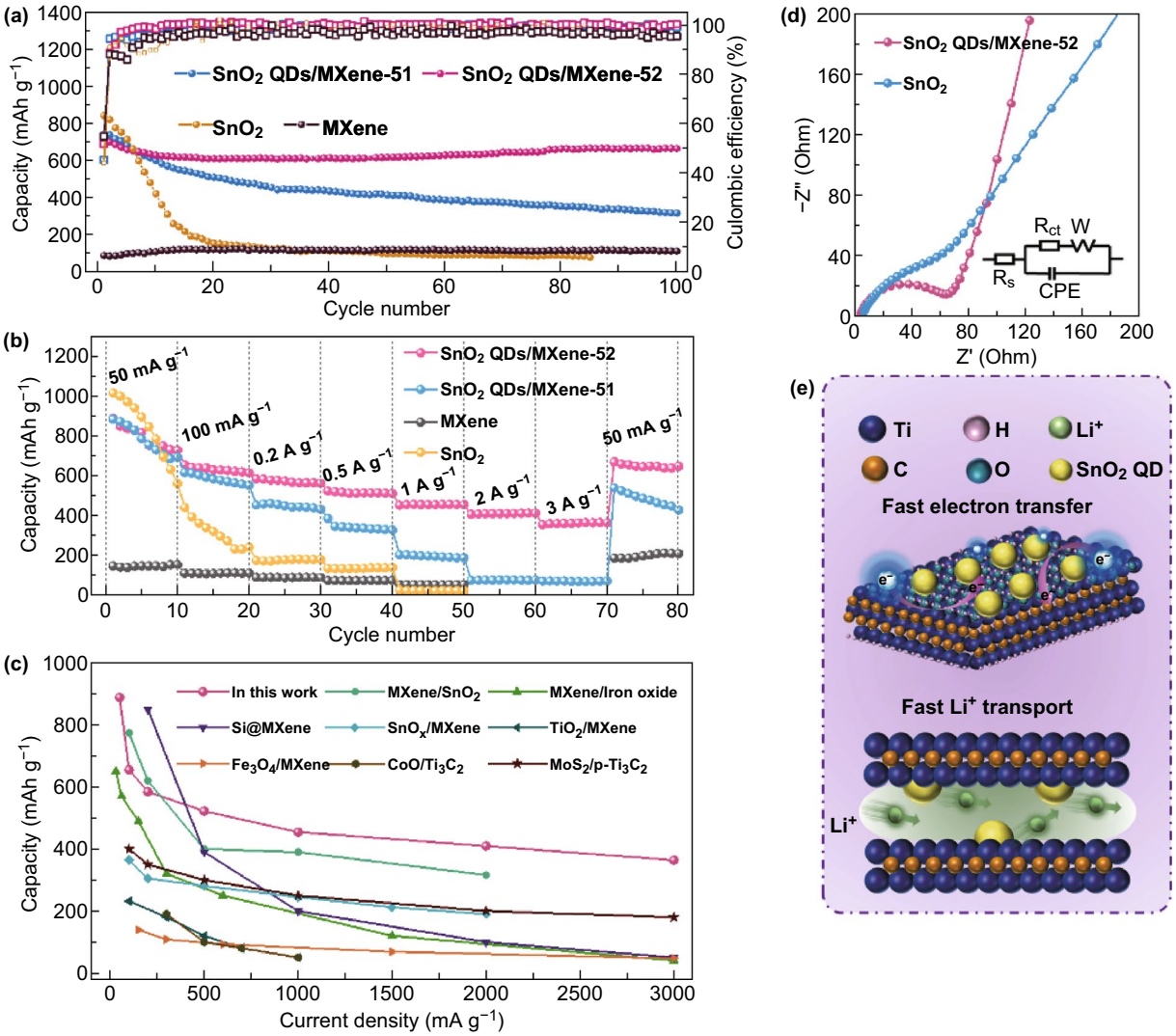

Fig. 5 **a** Cycle stability, **b** rate performance of all the samples as LIB electrodes. **c** Comparison of rate capacity between the SnO_2 QDs/MXene-52 and other MXene-based electrode materials reported for LIBs. **d** Nyquist plots of the SnO_2 QDs/MXene-52 and the pure SnO_2 electrodes; **e** energy storage mechanism of the 0D–2D SnO_2 QDs/MXene hybrids

© The authors
https://doi.org/10.1007/s40820-019-0296-7

the SnO_2 QDs/MXene electrode exhibit much enhanced rate capability compared to pure SnO_2 QDs. Especially for SnO_2 QDs/MXene-52, as the current density increases from 50 to 100, 200, 500, 1000, 2000, and 3000 mA g^{-1}, its reversible capacity remains 887.4, 655.2, 584.5, 522.0, 454.7, 409.7, and 364.0 mAh g^{-1}, respectively, demonstrating superior rate performance. When the current density returns back to 50 mA g^{-1} again, the capacity recovers to 688.1 mAh g^{-1}. These results indicate that the unique 0D–2D architecture of the SnO_2 QDs/MXene hybrids facilitates the Li ion diffusion and the electron transfer, thereby enhancing the reaction kinetics and the rate capability. The comparison of the rate performance for QDs/MXene-52 with previously reported SnO_2-based anodes and other MXene-based anodes is plotted in Fig. 5c. The SnO_2 QDs/MXene-52 demonstrate superior rate capability compared to other anode materials based on MXene matrix, such as SnO_2 QDs/MXene backbone [40], SnO_x nanosheets/MXene [54], Fe_2O_3/Mxene [37], Fe_3O_4 nanoparticles@MXene [50], TiO_2 nanowire/Ti_3C_2 [55], CoO nanoparticles/Ti_3C_2 [44], MoS_2/*p*-Ti_3C_2 [56], and Si@Ti_3C_2 [57] etc.

Electrochemical impedance spectroscopy was employed to compare the reaction kinetics of the SnO_2 QDs/MXene-52 and the bare SnO_2 QDs. The typical Nyquist plots of the two electrodes (Fig. 5d) consist of a compressed semicircle in the intermediate frequency region and a diagonal line in the low frequency range. The semicircle is related to the charge transfer resistance (R_{ct}), and the oblique line is related to Warburg impedance, suggesting the diffusion of Li ion in the active materials [58]. The R_{ct} values of the SnO_2 QDs/MXene-52 and SnO_2 QDs electrode were calculated to be 75.50 and 100.20 Ω, respectively. Obviously, SnO_2 QDs/MXene-52 possesses much lower R_{ct} value compared to bare SnO_2 QDs. This can be attributed to the high electrical conductivity of the MXene and the fast charge diffusion reaction due to its unique 0D–2D structure. Moreover, the SnO_2 QDs/MXene-52 shows a relatively steep low-frequency tail, indicative of high Li ion diffusibility, which results from the efficient ion transfer pathways constructed by MXene.

The above excellent electrochemical performances are because of the synergic effect between MXene nanosheets and SnO_2 QDs, and the mechanism is illustrated in Fig. 5e. In the SnO_2 QDs/MXene hybrids, the MXene nanosheets act as 2D substrates for uniform anchoring of SnO_2 QDs. The MXene nanosheets prevent the aggregation of SnO_2 QDs and work as an elastic buffer space to adapt to the volume expansion/contraction of SnO_2 QDs during charging and discharging, thus leading to good cycle stability. Furthermore, MXene nanosheets with good electric conductivity construct effective conductive channels for SnO_2 QDs, facilitating fast charge transport and improving the rate performance. Moreover, the unique 0D–2D structure offers massive electrochemically active sites for high specific capacity, which contribute in improving the electrochemical performance of electrode materials, thus excellent lithium-ion storage performances are obtained for SnO_2 QDs/MXene hybrids.

4 Conclusions

The 0D–2D SnO_2 QDs/MXene hybrids have been successfully synthesized by an efficient electrostatic self-assembly strategy. The 0D SnO_2 QDs with an average size of 4.7 nm are uniformly distributed on the 2D MXene nanosheets with strong adhesion, acting as structurally stable host for lithium storage. The 2D MXene nanosheets buffer the volume change of SnO_2 QDs during charge/discharge and construct effective channels for charge transport. Besides this, the 0D–2D structure creates additional active sites. The 2D conductive $Ti_3C_2T_x$ MXene, ultra-small SnO_2 QDs, and unique 0D–2D nanoarchitecture are synergistically responsible for the outstanding electrochemical performances of the SnO_2 QDs/MXene hybrids. As an anode for LIBs, it exhibits a high specific capacity of 887.4 mAh g^{-1} at 50 mA g^{-1}, excellent rate capability (364 mAh g^{-1} at 3 A g^{-1}), and superior cycle stability (659.8 mAh g^{-1} after 100 cycles with 91% retention). These results indicate that the 0D–2D SnO_2 QDs/MXene is a promising anode material for advanced LIBs. In addition, the electrostatic self-assembly method could be extended to other transition metal oxide/MXene hybrids and will have potential applications in sodium-ion batteries, potassium-ion batteries, and supercapacitors.

Acknowledgements This work was supported by the National Key Research and Development Program of China "New Energy Project for Electric Vehicle" (2016YFB0100204), the National Natural Science Foundation of China (Nos. 51772030, 21805011, 51572011, 51802012), the Joint Funds of the National Natural Science Foundation of China (U1564206) and Beijing Key Research

and Development Plan (Z181100004518001) and China Postdoctoral Science Foundation (Nos. 2017M620637, 2018M643697, 2019T120930).

Open Access This article is distributed under the terms of the Creative Commons Attribution 4.0 International License (http://creativecommons.org/licenses/by/4.0/), which permits unrestricted use, distribution, and reproduction in any medium, provided you give appropriate credit to the original author(s) and the source, provide a link to the Creative Commons license, and indicate if changes were made.

Electronic supplementary material The online version of this article (https://doi.org/10.1007/s40820-019-0296-7) contains supplementary material, which is available to authorized users.

References

1. M. Li, J. Lu, Z. Chen, K. Amine, 30 years of lithium-ion batteries. Adv. Mater. **30**(33), 1800561 (2018). https://doi.org/10.1002/adma.201800561
2. X. Zuo, J. Zhu, P. Müller-Buschbaum, Y.-J. Cheng, Silicon based lithium-ion battery anodes: a chronicle perspective review. Nano Energy **31**, 113–143 (2017). https://doi.org/10.1016/j.nanoen.2016.11.013
3. H. Liu, M. Jia, Q. Zhu, B. Cao, R. Chen, Y. Wang, F. Wu, B. Xu, 3D–0D graphene-Fe_3O_4 quantum dot hybrids as high-performance anode materials for sodium-ion batteries. ACS Appl. Mater. Interfaces **8**(40), 26878–26885 (2016). https://doi.org/10.1021/acsami.6b09496
4. Y. Zhao, X. Li, B. Yan, D. Xiong, D. Li, S. Lawes, X. Sun, Recent developments and understanding of novel mixed transition-metal oxides as anodes in lithium ion batteries. Adv. Energy Mater. **6**(8), 1502175 (2016). https://doi.org/10.1002/aenm.201502175
5. P. Lian, J. Wang, D. Cai, G. Liu, Y. Wang, H. Wang, Design and synthesis of porous nano-sized Sn@C/graphene electrode material with 3D carbon network for high-performance lithium-ion batteries. J. Alloys Compd. **604**, 188–195 (2014). https://doi.org/10.1016/j.jallcom.2014.03.116
6. J. Mao, T. Zhou, Y. Zheng, H. Gao, H.K. Liu, Z. Guo, Two-dimensional nanostructures for sodium-ion battery anodes. J. Mater. Chem. A **6**(8), 3284–3303 (2018). https://doi.org/10.1039/c7ta10500b
7. L. Fei, Y. Jiang, Y. Xu, G. Chen, Y. Li, X. Xu, S. Deng, H. Luo, A novel solvent-free thermal reaction of ferrocene and sulfur for one-step synthesis of iron sulfide and carbon nanocomposites and their electrochemical performance. J. Power Sources **265**, 1–5 (2014). https://doi.org/10.1016/j.jpowsour.2014.04.110
8. T. Zhou, W.K. Pang, C. Zhang, J. Yang, Z. Chen, H.K. Liu, Z. Guo, Enhanced sodium-ion battery performance by structural phase transition from two-dimensional hexagonal-SnS_2 to orthorhombic-SnS. ACS Nano **8**(8), 8323–8333 (2014). https://doi.org/10.1021/nn503582c
9. S.L. Zhang, B.Y. Guan, H.B. Wu, X.W.D. Lou, Metal-organic framework-assisted synthesis of compact Fe_2O_3 nanotubes in Co_3O_4 host with enhanced lithium storage properties. Nano Micro Lett. **10**(3), 44 (2018). https://doi.org/10.1007/s40820-018-0197-1
10. A. Bai, L. Wang, J. Li, X. He, J. Wang, J. Wang, Composite of graphite/phosphorus as anode for lithium-ion batteries. J. Power Sources **289**, 100–104 (2015). https://doi.org/10.1016/j.jpowsour.2015.04.168
11. X. Yu, H.J. Kim, J.-Y. Hong, Y.M. Jung, K.D. Kwon, J. Kong, H.S. Park, Elucidating surface redox charge storage of phosphorus-incorporated graphenes with hierarchical architectures. Nano Energy **15**, 576–586 (2015). https://doi.org/10.1016/j.nanoen.2015.05.010
12. W. Zhang, W.K. Pang, V. Sencadas, Z. Guo, Understanding high-energy-density Sn_4P_3 anodes for potassium-ion batteries. Joule **2**(8), 1534–1547 (2018). https://doi.org/10.1016/j.joule.2018.04.022
13. L. Pan, Y. Zhang, F. Lu, Y. Du, Z. Lu et al., Exposed facet engineering design of graphene-SnO_2 nanorods for ultrastable Li-ion batteries. Energy Storage Mater. (2018). https://doi.org/10.1016/j.ensm.2018.10.007
14. H. Wang, X. Jiang, Y. Chai, X. Yang, R. Yuan, Sandwich-like C@SnO_2/Sn/void@C hollow spheres as improved anode materials for lithium ion batteries. J. Power Sources **379**, 191–196 (2018). https://doi.org/10.1016/j.jpowsour.2018.01.054
15. B. Zhao, Z. Wang, S. Wang, J. Jiang, J. Si, S. Huang, Z. Chen, W. Li, Y. Jiang, Sandwiched spherical tin dioxide/graphene with a three-dimensional interconnected closed pore structure for lithium storage. Nanoscale **10**(34), 16116–16126 (2018). https://doi.org/10.1039/c8nr03776k
16. P. Deng, J. Yang, S. Li, T.-E. Fan, H.-H. Wu et al., High initial reversible capacity and long life of ternary SnO_2-Co-carbon nanocomposite anodes for lithium-ion batteries. Nano Micro Lett. **11**, 18 (2019). https://doi.org/10.1007/s40820-019-0246-4
17. J. Liang, C. Yuan, H. Li, K. Fan, Z. Wei, H. Sun, J. Ma, Growth of SnO_2 nanoflowers on N-doped carbon nanofibers as anode for Li- and Na-ion batteries. Nano Micro Lett. **10**(2), 21 (2018). https://doi.org/10.1007/s40820-017-0172-2
18. H. Li, Q. Su, J. Kang, M. Huang, M. Feng, H. Feng, P. Huang, G. Du, Porous SnO_2 hollow microspheres as anodes for high-performance lithium ion battery. Mater. Lett. **217**, 276–280 (2018). https://doi.org/10.1016/j.matlet.2018.01.015
19. Y.T. Liu, P. Zhang, N. Sun, B. Anasori, Q.Z. Zhu, H. Liu, Y. Gogotsi, B. Xu, Self-assembly of transition metal oxide nanostructures on MXene nanosheets for fast and stable lithium storage. Adv. Mater. **30**(23), 1707334 (2018). https://doi.org/10.1002/adma.201707334
20. S. Abouali, M. Akbari Garakani, J.-K. Kim, Ultrafine SnO_2 nanoparticles encapsulated in ordered mesoporous carbon framework for Li-ion battery anodes. Electrochim. Acta **284**, 436–443 (2018). https://doi.org/10.1016/j.electacta.2018.07.162

21. N. Hu, X. Lv, Y. Dai, L. Fan, D. Xiong, X. Li, SnO_2/reduced graphene oxide interlayer mitigating the shuttle effect of Li-S batteries. ACS Appl. Mater. Interfaces **10**(22), 18665–18674 (2018). https://doi.org/10.1021/acsami.8b03255
22. J. Abe, K. Takahashi, K. Kawase, Y. Kobayashi, S. Shiratori, Self-standing carbon nanofiber and SnO_2 nanorod composite as a high-capacity and high-rate-capability anode for lithium-ion batteries. ACS Appl. Nano Mater. **1**(6), 2982–2989 (2018). https://doi.org/10.1021/acsanm.8b00586
23. D. Ma, Y. Li, H. Mi, S. Luo, P. Zhang, Z. Lin, J. Li, H. Zhang, Robust SnO_{2-x} nanoparticle-impregnated carbon nanofibers with outstanding electrochemical performance for advanced sodium-ion batteries. Angew. Chem. Int. Ed. **57**(29), 8901–8905 (2018). https://doi.org/10.1002/anie.201802672
24. R. Jia, J. Yue, Q. Xia, J. Xu, X. Zhu, S. Sun, T. Zhai, H. Xia, Carbon shelled porous $SnO_{2-\delta}$ nanosheet arrays as advanced anodes for lithium-ion batteries. Energy Storage Mater. **13**, 303–311 (2018). https://doi.org/10.1016/j.ensm.2018.02.009
25. Y. Cheng, J. Huang, H. Qi, L. Cao, J. Yang, Q. Xi, X. Luo, K. Yanagisawa, J. Li, Adjusting the chemical bonding of SnO_2@CNT composite for enhanced conversion reaction kinetics. Small **13**(31), 1700656 (2017). https://doi.org/10.1002/smll.201700656
26. Y. Cheng, J. Huang, H. Qi, L. Cao, X. Luo, J. Li, Z. Xu, J. Yang, Controlling the Sn-C bonds content in SnO_2@CNTs composite to form in situ pulverized structure for enhanced electrochemical kinetics. Nanoscale **9**(47), 18681–18689 (2017). https://doi.org/10.1039/c7nr05556k
27. P. Simon, Two-dimensional MXene with controlled interlayer spacing for electrochemical energy storage. ACS Nano **11**(3), 2393–2396 (2017). https://doi.org/10.1021/acsnano.7b01108
28. L. Yu, L. Hu, B. Anasori, Y.-T. Liu, Q. Zhu, P. Zhang, Y. Gogotsi, B. Xu, MXene-bonded activated carbon as a flexible electrode for high-performance supercapacitors. ACS Energy Lett. **3**(7), 1597–1603 (2018). https://doi.org/10.1021/acsenergylett.8b00718
29. C.J. Zhang, S.J. Kim, M. Ghidiu, M.-Q. Zhao, M.W. Barsoum, V. Nicolosi, Y. Gogotsi, Layered orthorhombic Nb_2O_5@$Nb_4C_3T_x$ and TiO_2@$Ti_3C_2T_x$ hierarchical composites for high performance Li-ion batteries. Adv. Funct. Mater. **26**(23), 4143–4151 (2016). https://doi.org/10.1002/adfm.201600682
30. C. Zhang, M. Beidaghi, M. Naguib, M.R. Lukatskaya, M.-Q. Zhao et al., Synthesis and charge storage properties of hierarchical niobium pentoxide/carbon/niobium carbide (MXene) hybrid materials. Chem. Mater. **28**(11), 3937–3943 (2016). https://doi.org/10.1021/acs.chemmater.6b01244
31. C.J. Zhang, S. Pinilla, N. McEvoy, C.P. Cullen, B. Anasori et al., Oxidation stability of colloidal two-dimensional titanium carbides (MXenes). Chem. Mater. **29**(11), 4848–4856 (2017). https://doi.org/10.1021/acs.chemmater.7b00745
32. M.Q. Zhao, C.E. Ren, Z. Ling, M.R. Lukatskaya, C. Zhang et al., Flexible MXene/carbon nanotube composite paper with high volumetric capacitance. Adv. Mater. **27**(2), 339–345 (2015). https://doi.org/10.1002/adma.201404140
33. X. Xie, S. Wang, K. Kretschmer, G. Wang, Two-dimensional layered compound based anode materials for lithium-ion batteries and sodium-ion batteries. J. Colloid Interface Sci. **499**, 17–32 (2017). https://doi.org/10.1016/j.jcis.2017.03.077
34. X. Xie, M.-Q. Zhao, B. Anasori, K. Maleski, C.E. Ren et al., Porous heterostructured MXene/carbon nanotube composite paper with high volumetric capacity for sodium-based energy storage devices. Nano Energy **26**, 513–523 (2016). https://doi.org/10.1016/j.nanoen.2016.06.005
35. C.J. Zhang, S.H. Park, A. Seral-Ascaso, S. Barwich, N. McEvoy et al., High capacity silicon anodes enabled by MXene viscous aqueous ink. Nat. Commun. **10**(1), 849 (2019). https://doi.org/10.1038/s41467-019-08383-y
36. G. Zou, Z. Zhang, J. Guo, B. Liu, Q. Zhang, C. Fernandez, Q. Peng, Synthesis of MXene/Ag composites for extraordinary long cycle lifetime lithium storage at high rates. ACS Appl. Mater. Interfaces **8**(34), 22280–22286 (2016). https://doi.org/10.1021/acsami.6b08089
37. A. Ali, K. Hantanasirisakul, A. Abdala, P. Urbankowski, M.Q. Zhao, B. Anasori, Y. Gogotsi, B. Aissa, K.A. Mahmoud, Effect of synthesis on performance of MXene/iron oxide anode material for lithium-ion batteries. Langmuir **34**(38), 11325–11334 (2018). https://doi.org/10.1021/acs.langmuir.8b01953
38. M.-Q. Zhao, M. Torelli, C.E. Ren, M. Ghidiu, Z. Ling, B. Anasori, M.W. Barsoum, Y. Gogotsi, 2D titanium carbide and transition metal oxides hybrid electrodes for Li-ion storage. Nano Energy **30**, 603–613 (2016). https://doi.org/10.1016/j.nanoen.2016.10.062
39. C. Chen, X. Xie, B. Anasori, A. Sarycheva, T. Makaryan et al., MoS_2-on-MXene heterostructures as highly reversible anode materials for lithium-ion batteries. Angew. Chem. Int. Ed. **57**(7), 1846–1850 (2018). https://doi.org/10.1002/anie.201710616
40. J. Xiong, L. Pan, H. Wang, F. Du, Y. Chen, J. Yang, C. Zhang, Synergistically enhanced lithium storage performance based on titanium carbide nanosheets (MXene) backbone and SnO_2 quantum dots. Electrochim. Acta **268**, 503–511 (2018). https://doi.org/10.1016/j.electacta.2018.02.090
41. M. Boota, B. Anasori, C. Voigt, M.Q. Zhao, M.W. Barsoum, Y. Gogotsi, Pseudocapacitive electrodes produced by oxidant-free polymerization of pyrrole between the layers of 2D titanium carbide (MXene). Adv. Mater. **28**(7), 1517–1522 (2016). https://doi.org/10.1002/adma.201504705
42. X. Lu, H. Wang, Z. Wang, Y. Jiang, D. Cao, G. Yang, Room-temperature synthesis of colloidal SnO_2 quantum dot solution and ex situ deposition on carbon nanotubes as anode materials for lithium ion batteries. J. Alloys Compd. **680**, 109–115 (2016). https://doi.org/10.1016/j.jallcom.2016.04.128
43. J. Yan, C.E. Ren, K. Maleski, C.B. Hatter, B. Anasori, P. Urbankowski, A. Sarycheva, Y. Gogotsi, Flexible MXene/graphene films for ultrafast supercapacitors with outstanding volumetric capacitance. Adv. Funct. Mater. **27**(30), 1701264 (2017). https://doi.org/10.1002/adfm.201701264
44. X. Li, J. Zhu, Y. Fang, W. Lv, F. Wang, Y. Liu, H. Liu, Hydrothermal preparation of CoO/Ti_3C_2 composite material for lithium-ion batteries with enhanced electrochemical performance. J. Electroanal. Chem. **817**, 1–8 (2018). https://doi.org/10.1016/j.jelechem.2018.03.031

45. H. Zhang, P. Zhang, W. Zheng, W. Tian, J. Chen, Y. Zhang, Z. Sun, 3D d-Ti_3C_2 xerogel framework decorated with core-shell SnO_2@C for high-performance lithium-ion batteries. Electrochim. Acta **285**, 94–102 (2018). https://doi.org/10.1016/j.electacta.2018.07.198
46. M. Sahoo, S. Ramaprabhu, One-pot environment-friendly synthesis of boron doped graphene-SnO_2 for anodic performance in Li ion battery. Carbon **127**, 627–635 (2018). https://doi.org/10.1016/j.carbon.2017.11.056
47. Z. Ma, X. Zhou, W. Deng, D. Lei, Z. Liu, 3D porous MXene (Ti_3C_2)/reduced graphene oxide hybrid films for advanced lithium storage. ACS Appl. Mater. Interfaces **10**(4), 3634–3643 (2018). https://doi.org/10.1021/acsami.7b17386
48. W. Bao, X. Xie, J. Xu, X. Guo, J. Song, W. Wu, D. Su, G. Wang, Confined sulfur in 3D MXene/reduced graphene oxide hybrid nanosheets for lithium-sulfur battery. Chemistry **23**(51), 12613–12619 (2017). https://doi.org/10.1002/chem.201702387
49. J. Zhu, Y. Tang, C. Yang, F. Wang, M. Cao, Composites of TiO_2 nanoparticles deposited on Ti_3C_2 MXene nanosheets with enhanced electrochemical performance. J. Electrochem. Soc. **163**(5), A785–A791 (2016). https://doi.org/10.1149/2.0981605jes
50. Y. Wang, Y. Li, Z. Qiu, X. Wu, P. Zhou et al., Fe_3O_4@Ti_3C_2 MXene hybrids with ultrahigh volumetric capacity as an anode material for lithium-ion batteries. J. Mater. Chem. A **6**(24), 11189–11197 (2018). https://doi.org/10.1039/c8ta00122g
51. X. Ao, J. Jiang, Y. Ruan, Z. Li, Y. Zhang, J. Sun, C. Wang, Honeycomb-inspired design of ultrafine SnO_2@C nanospheres embedded in carbon film as anode materials for high performance lithium- and sodium-ion battery. J. Power Sources **359**, 340–348 (2017). https://doi.org/10.1016/j.jpowsour.2017.05.064
52. D. Cui, Z. Zheng, X. Peng, T. Li, T. Sun, L. Yuan, Fluorine-doped SnO_2 nanoparticles anchored on reduced graphene oxide as a high-performance lithium ion battery anode. J. Power Sources **362**, 20–26 (2017). https://doi.org/10.1016/j.jpowsour.2017.07.024
53. X. Wang, X. Zhou, K. Yao, J. Zhang, Z. Liu, A SnO_2/graphene composite as a high stability electrode for lithium ion batteries. Carbon **49**(1), 133–139 (2011). https://doi.org/10.1016/j.carbon.2010.08.052
54. X. Sun, Y. Liu, J. Zhang, L. Hou, J. Sun, C. Yuan, Facile construction of ultrathin snox nanosheets decorated MXene (Ti_3C_2) nanocomposite towards Li-ion batteries as high performance anode materials. Electrochim. Acta **295**, 237–245 (2019). https://doi.org/10.1016/j.electacta.2018.10.152
55. W. Lv, J. Zhu, F. Wang, Y. Fang, Facile synthesis and electrochemical performance of TiO_2 nanowires/Ti_3C_2 composite. J. Mater. Sci. **29**(6), 4881–4887 (2018). https://doi.org/10.1007/s10854-017-8446-5
56. M. Zheng, R. Guo, Z. Liu, B. Wang, L. Meng, F. Li, T. Li, Y. Luo, MoS_2 intercalated *p*-Ti_3C_2 anode materials with sandwich-like three dimensional conductive networks for lithium-ion batteries. J. Alloys Compd. **735**, 1262–1270 (2018). https://doi.org/10.1016/j.jallcom.2017.11.250
57. F. Kong, X. He, Q. Liu, X. Qi, D. Sun, Y. Zheng, R. Wang, Y. Bai, Enhanced reversible Li-ion storage in Si@Ti_3C_2 MXene nanocomposite. Electrochem. Commun. **97**, 16–21 (2018). https://doi.org/10.1016/j.elecom.2018.10.003
58. B. Cao, Q. Zhang, H. Liu, B. Xu, S. Zhang et al., Graphitic carbon nanocage as a stable and high power anode for potassium-ion batteries. Adv. Energy Mater. **8**(25), 1801149 (2018). https://doi.org/10.1002/aenm.201801149

© The authors https://doi.org/10.1007/s40820-019-0296-7